New effective interactions in relativistic mean field theory with nonlinear terms and density-dependent meson-nucleon coupling

Wenhui Long,[1,2] Jie Meng,[1,3,4,*] Nguyen Van Giai,[2] and Shan-Gui Zhou[1,5,3,4]
[1]*School of Physics, Peking University, 100871 Beijing, China*
[2]*Institut de Physique Nucléaire, CNRS-IN2P3, Université Paris-Sud, 91406 Orsay, France*
[3]*Institute of Theoretical Physics, Chinese Academy of Sciences, 100080 Beijing, China*
[4]*Center of Theoretical Nuclear Physics, National Laboratory of Heavy Ion Accelerator, 730000 Lanzhou, China*
[5]*Max-Planck-Institut für Kernphysik, 69029 Heidelberg, Germany*
(Received 1 November 2003; published 17 March 2004)

New parameter sets for the Lagrangian density in the relativistic mean field (RMF) theory, PK1 with nonlinear σ- and ω-meson self-coupling, PK1R with nonlinear σ-, ω-, and ρ-meson self-coupling, and PKDD with the density-dependent meson-nucleon coupling are proposed. They are able to provide an excellent description not only for the properties of nuclear matter but also for the nuclei in and far from the valley of β stability. For the first time in the parametrization of the RMF Lagrangian density, the center-of-mass correction is treated by a microscopic way, which is essential to unify the description of nuclei from light to heavy regions with one effective interaction.

DOI: 10.1103/PhysRevC.69.034319 PACS number(s): 21.30.Fe, 21.60.Jz, 21.10.Dr

I. INTRODUCTION

In the past decade, the development of unstable nuclear beams [1,2] has extended our knowledge of nuclear physics from the stable nuclei and those nearby to the unstable nuclei far from the stability line. Intense research in this area shows that there exist lots of unexpected phenomena: strange nuclear structure such as neutron halo (skin) and proton halo (skin) [3–10], soft excitation modes [11,12], the enhancement of fusion cross sections induced by the extended matter distributions [13,14], etc. With further developments, many other new features will be found. It also becomes very important to find a reliable theory and improve the reliability for predicting the properties of even more exotic nuclei out to the proton and neutron drip lines.

Relativistic mean field (RMF) [15,16] theory has received wide attention because of its successful description of many nuclear phenomena during the past years. With a very limited number of parameters, RMF theory is able to give a satisfactory description for the ground state properties of spherical [17] and deformed nuclei [18] at and away from the stability line. The recent reviews on RMF theory can be seen in Refs. [16–18]. In the simplest version of RMF theory, the mesons do not interact among themselves, which results in a too large incompressibility for nuclear matter. Boguta and Bodmer [19] therefore proposed to include a nonlinear self-coupling of the σ field, a concept which has been used in almost all the recent applications. The meson self-coupling introduces a new density dependence into the Lagrangian and, consequently, the nuclear matter incompressibility can be lowered to reasonable values. As an implement, in 1994 the nonlinear self-coupling of the ω field is introduced by Sugahara and Toki [20]. In this paper we will introduce the nonlinear self-coupling for the ρ field. Recently RMF theory with density-dependent (DD) meson-nucleon couplings [21–27] was developed by various authors. Several applications to different systems such as neutron star [28,29], supernova [30], and hypernuclei [31] have subsequently been performed.

Till now the two versions (the nonlinear self-coupling of meson fields and the DD meson-nucleon couplings) of RMF theory have been successfully applied to describe the nuclear properties, including binding energies, nuclear matter distribution, single-particle spectra, magnetic moments, collective excited states, dipole sum rule, shell effects in finite nuclei, pseudospin symmetry, rotating nuclei, superdeformed bands, etc. In particular, the halo phenomena can be understood self-consistently in this microscopical model after the proper treatment of the continuum effect [7,32]. Combining with Glauber model, the charge-changing cross sections for C, N, O, and F isotopes are calculated and a good agreement with the data has been achieved [9,10]. The long existing problem for the origin of pseudospin symmetry in nuclei is given naturally as a relativistic symmetry [33–35]. A good agreement with experimental data has also been found recently for magnetic rotation [36], collective excitations such as giant resonances [37], and for twin bands in rotating superdeformed nuclei [38]. It is also noted that cranked RMF theory provides an excellent description of superdeformed rotational bands in the $A=140-150$ region [39], in the Sr region [40], and in the Hg region [41].

Among the existing parametrizations for RMF theory, the most frequently used are NL1 [42], PL-40 [43], NL-SH [44], TM1 [20], and NL3 [45] with nonlinear self-coupling of mesons, and TW99 [24] and DD-ME1 [25] with DD meson-nucleon coupling. The effective interactions NL1, NL3, TM1, NL-SH and TW99, DD-ME1 give good results in most of the cases.

Along the β stability line NL1 gives excellent results for binding energies and charge radii; in addition it provides an excellent description of the superdeformed bands [39,40].

*Electronic address: mengj@pku.edu.cn

However, in going away from the stability line the results are less satisfactory. This can be partly attributed to the large asymmetry energy $J \simeq 44$ MeV predicted by this force. In addition, the calculated neutron skin thickness shows systematic deviations from the experimental values for the set NL1.

In the effective interaction NL-SH this problem was treated in a better way and the improved isovector properties have been obtained with an asymmetry energy of $J \simeq 36$ MeV. Moreover, NL-SH seems to describe the deformation properties in a better way than NL1. However, the NL-SH parametrization produces a slight overbinding along the line of β stability, and in addition it fails to reproduce successfully the superdeformed minima in Hg isotopes in constrained calculations for the energy landscape. A remarkable disagreement between the two parametrizations is the quite different values predicted for the nuclear matter incompressibility. NL1 predicts a small value ($K=212$ MeV) while with NL-SH a very large value ($K=355$ MeV) is obtained. Both forces fail to reproduce the experimental values for the isoscalar giant monopole resonances for Pb and Zr nuclei. The NL1 parametrization underestimates the empirical data by about 2 MeV while NL-SH overestimates it by about the similar values. As an improvement, the effective interactions NL3 and TM1 provide reasonable compression modulus ($K_{\mathrm{NL3}}=268.0$ MeV, $K_{\mathrm{TM1}}=281.16$ MeV) and asymmetry energy ($J_{\mathrm{NL3}}=36.56$ MeV, $J_{\mathrm{TM1}}=36.89$ MeV) but fairly small baryonic saturation density ($\rho_{\mathrm{NL3}}=0.145, \rho_{\mathrm{TM1}}=0.145$). In order to improve the description of these quantities, we developed two nonlinear self-coupling parametrizations called as PK1 with nonlinear σ- and ω-meson nonlinear self-coupling, and PK1R with nonlinear σ-, ω-, and ρ-meson nonlinear self-coupling.

RMF theory with DD meson-nucleon couplings [22,23] is an alternative approach to the description of nuclear matter and finite nuclei as compared to the model with the nonlinear self-interactions of mesons. There exist two representative parametrizations TW99 [24] and DD-ME1 [25] for the density dependence of meson-nucleon coupling. They are able to describe quantitatively properties of nuclear matter and finite nuclei with similar quality as the parametrizations of the nonlinear self-coupling. As a comparison with the nonlinear self-coupling, we also developed a parametrization named as PKDD with DD meson-nucleon couplings.

In all previous nonlinear self-coupling parametrizations as mentioned above, the center-of-mass correction is made by a phenomenological way. In the present parametrizations, the PK series, the contribution from the center-of-mass motion is treated in a microscopic way [46]. The systematic behavior of the center-of-mass correction on nuclear masses is shown in Fig. 1. From this graph, we can see that it is essential to choose a proper method to treat the center-of-mass motion for both light and heavy nuclei. Obviously, the microscopic method provides more reasonable and reliable results for the center-of-mass motion (for the details, see Sec. III).

In Sec. II, we will present a short summary of RMF theory with the nonlinear self-coupling of meson fields and with DD meson-nucleon coupling and the relationship between them. The details of our parametrizations are given in Sec. III. In Secs. IV and V, we study the bulk properties of nuclear matter and spherical nuclei with the newly obtained effective interactions. The detailed microscopic structure of doubly magic nuclei is also investigated in the end of Sec. V. Finally conclusions are given in Sec. VI.

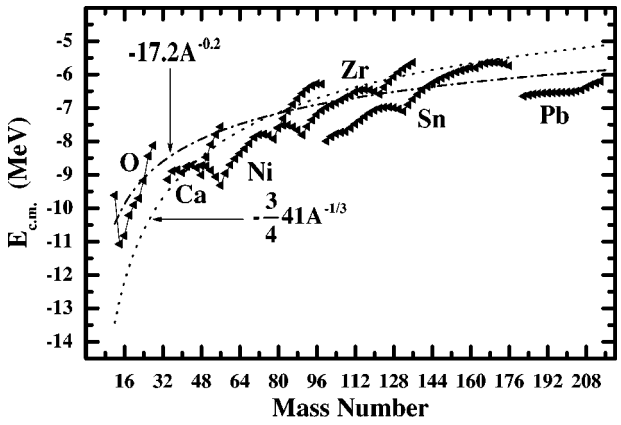

FIG. 1. The microscopic center-of-mass correction, in comparison with two phenomenological cases.

II. RMF THEORY WITH NONLINEAR SELF-COUPLING AND DENSITY-DEPENDENT MESON-NUCLEON COUPLING

A. Lagrangian density

The basic ansatz of the RMF theory [16] is a Lagrangian density whereby nucleons are described as Dirac particles which interact via the exchange of various mesons and the photon. The mesons considered are the scalar sigma (σ), vector omega (ω), and isovector vector rho ($\vec{\rho}$). The latter provides the necessary isospin asymmetry. The Lagrangian then consists of the free baryon and meson parts and the interaction part with minimal coupling, together with the nucleon mass M and m_σ (g_σ), m_ω (g_ω), and m_ρ (g_ρ) the masses (coupling constants) of the respective mesons:

$$\begin{aligned}\mathcal{L} = \bar{\psi}\Big\{ & i\gamma^\mu\partial_\mu - M - g_\sigma\sigma - g_\omega\gamma^\mu\omega_\mu - g_\rho\gamma^\mu\vec{\tau}\cdot\vec{\rho}_\mu \\ & - e\gamma^\mu\frac{1-\tau_3}{2}A_\mu\Big\}\psi + \tfrac{1}{2}\partial^\mu\sigma\partial_\mu\sigma - \tfrac{1}{2}m_\sigma^2\sigma^2 - \tfrac{1}{3}g_2\sigma^3 - \tfrac{1}{4}g_3\sigma^4 \\ & - \tfrac{1}{4}\omega^{\mu\nu}\omega_{\mu\nu} + \tfrac{1}{2}m_\omega^2\omega^\mu\omega_\mu + \tfrac{1}{4}c_3(\omega^\mu\omega_\mu)^2 - \tfrac{1}{4}\vec{\rho}^{\mu\nu}\cdot\vec{\rho}_{\mu\nu} \\ & + \tfrac{1}{2}m_\rho^2\vec{\rho}^\mu\cdot\vec{\rho}_\mu + \tfrac{1}{4}d_3(\vec{\rho}^\mu\cdot\vec{\rho}_\mu)^2 - \tfrac{1}{4}A^{\mu\nu}A_{\mu\nu}, \end{aligned} \tag{1}$$

where the tensor quantities are

$$\omega^{\mu\nu} = \partial^\mu\omega^\nu - \partial^\nu\omega^\mu, \tag{2a}$$

$$\vec{\rho}^{\mu\nu} = \partial^\mu\vec{\rho}^\nu - \partial^\nu\vec{\rho}^\mu + g_\rho\vec{\rho}^\mu\times\vec{\rho}^\nu, \tag{2b}$$

$$A^{\mu\nu} = \partial^\mu A^\nu - \partial^\nu A^\mu. \tag{2c}$$

In this paper we use arrow for isospin vectors and bold type for space vectors. There are 11 parameters in the Lagrangian density (1), i.e., four masses ($M, m_\sigma, m_\omega, m_\rho$), three nucleon-

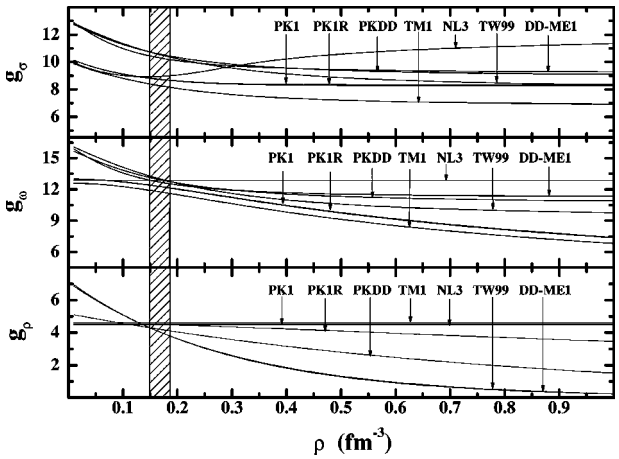

FIG. 2. The meson-nucleon coupling constants as a function of baryonic density in nuclear matter. The density dependence of g_ρ for PK1R corresponds to nonsymmetric nuclear matter ($N/Z=3$).

meson coupling constants ($g_\sigma, g_\omega, g_\rho$), and four self-coupling constants (g_2, g_3, c_3, d_3). Generally, the nucleon mass M and ρ-meson mass m_ρ (also sometimes the mass of ω meson in some parametrizations) are fixed to their free values and the nonlinear coupling coefficients c_3 and d_3 are taken as zeros. Then the remaining six to seven parameters are determined by the fitting to the experimental observables.

Different from the nonlinear self-coupling version, the meson-nucleon interactions are described as density dependent in the DD meson-nucleon coupling RMF theory [24,25]. The meson-nucleon coupling constants $g_\sigma, g_\omega, g_\rho$ become functions of the baryonic density ρ_v, $\rho_v = \sqrt{j_\mu j^\mu}$ where $j^\mu = \bar{\psi}\gamma^\mu\psi$ and the nonlinear self-coupling constants g_2, g_3, c_3, d_3 are set to zero in the Lagrangian density (1).

For σ and ω mesons, the baryonic density dependence of the coupling constants is adopted as

$$g_i(\rho_v) = g_i(\rho_{\rm sat}) f_i(x) \quad \text{for } i = \sigma, \omega, \tag{3}$$

where

$$f_i(x) = a_i \frac{1 + b_i(x + d_i)^2}{1 + c_i(x + d_i)^2} \tag{4}$$

is a function of $x = \rho_v/\rho_{\rm sat}$, and $\rho_{\rm sat}$ denotes the baryonic saturation density of nuclear matter.

For the ρ meson, an exponential dependence is utilized as

$$g_\rho = g_\rho(\rho_{\rm sat}) \exp[-a_\rho(x-1)]. \tag{5}$$

For the functions $f_i(x)$, one has five constraint conditions $f_i(1)=1$, $f''_\sigma(1) = f''_\omega(1)$, and $f''_0(0)=0$. Then eight parameters related to density dependence for σ-N and ω-N couplings are reduced to three free parameters. As mentioned above, the masses of nucleon and ρ meson are fixed in general, and the nonlinear self-coupling constants g_2, g_3, c_3, and d_3 are set to zero. With four free parameters for density dependence, there totally are eight to nine parameters left free in the Lagrangian density (1) for the density-dependent meson-nucleon coupling RMF theory.

B. Nuclear energy and self-energy

The single-nucleon Dirac equation is derived by the variation of the Lagrangian density (1) with respect to $\bar{\psi}$,

$$[i\gamma^\mu\partial_\mu - (M + \Sigma_S) - \gamma^\mu\Sigma_\mu]\psi = 0 \tag{6}$$

with the nucleon self-energies Σ_μ and Σ_S defined by the following relations:

$$\Sigma_S = g_\sigma\sigma, \tag{7a}$$

$$\Sigma_\mu = g_\omega\omega_\mu + g_\rho\vec{\tau}\cdot\vec{\rho}_\mu + e\frac{1-\tau_3}{2}A_\mu + \Sigma^R_\mu, \tag{7b}$$

where the rearrangement term Σ^R_μ comes from the density-dependence of the meson-nucleon coupling constants [22,23],

TABLE I. The nonlinear effective interactions PK1, PK1R, and density-dependent effective interactions PKDD. The masses (in MeV) and meson-nucleon couplings are shown in comparison with TM1 [20], NL3 [45], TW99 [24], and DD-ME1 [25].

	PK1	PK1R	PKDD	TM1	NL3	TW99	DD-ME1
M_n	939.5731	939.5731	939.5731	938	939	939	938.5000
M_p	938.2796	938.2796	938.2796	938	939	939	938.5000
m_σ	514.0891	514.0873	555.5112	511.198	508.1941	550	549.5255
m_ω	784.254	784.2223	783	783	782.501	783	783.0000
m_ρ	763	763	763	770	763	763	763.0000
g_σ	10.3222	10.3219	10.7385	10.0289	10.2169	10.7285	10.4434
g_ω	13.0131	13.0134	13.1476	12.6139	12.8675	13.2902	12.8939
g_ρ	4.5297	4.55	4.2998	4.6322	4.4744	3.661	3.8053
g_2	−8.1688	−8.1562	0	−7.2325	−10.4307	0	0.0000
g_3	−9.9976	−10.1984	0	0.6183	−28.8851	0	0.0000
c_3	55.636	54.4459	0	71.3075	0	0	0.0000
d_3	0	350	0	0	0	0	0

TABLE II. Density-dependent parameters of PKDD for meson-nucleon coupling in comparison with TW99 [24] and DD-ME1 [25].

	a_σ	b_σ	c_σ	d_σ	a_ω	b_ω	c_ω	d_ω	a_ρ
PKDD	1.327423	0.435126	0.691666	0.694210	1.342170	0.371167	0.611397	0.738376	0.183305
TW99	1.365469	0.226061	0.409704	0.901995	1.402488	0.172577	0.344293	0.983955	0.515000
DD-ME1	1.3854	0.9781	1.5342	0.4661	1.3879	0.8525	1.3566	0.4957	0.5008

$$\Sigma_R^\mu = \frac{j^\mu}{\rho_v}\left(\frac{\partial g_\omega}{\partial \rho_v}\overline{\psi}\gamma^\nu\psi\omega_\nu + \frac{\partial g_\rho}{\partial \rho_v}\overline{\psi}\gamma^\nu\vec{\tau}\psi\cdot\vec{\rho}_\nu + \frac{\partial g_\sigma}{\partial \rho_v}\overline{\psi}\psi\sigma\right), \tag{8}$$

which is reduced to zero in RMF theory with the nonlinear self-coupling.

The Klein-Gordon equations for mesons are obtained by the variation of the Lagrangian density (1) with respect to the corresponding meson field operators:

$$[-\Delta + m_\sigma^2]\sigma = -g_\sigma\rho_s - g_2\sigma^2 - g_3\sigma^3, \tag{9a}$$

$$[-\Delta + m_\omega^2]\omega = g_\omega\rho_b - c_3\omega^3, \tag{9b}$$

$$[-\Delta + m_\rho^2]\rho = g_\rho[\rho_b^{(n)} - \rho_b^{(p)}] - d_3\rho^3. \tag{9c}$$

For the RMF theory with the nonlinear self-coupling, the self-coupling of mesons can be expressed into the density-dependence of meson-nucleon coupling by redefining the coupling constants,

$$g_\sigma = g_\sigma + [g_2\sigma^2 + g_3\sigma^3]/\rho_s, \tag{10a}$$

$$g_\omega = g_\omega - c_3\omega^3/\rho_b, \tag{10b}$$

$$g_\rho = g_\rho - d_3\rho^3/[\rho_b^n - \rho_b^p]. \tag{10c}$$

The behaviors of the coupling constants with respect to the baryonic density are shown in Fig. 2.

TABLE III. Total binding energies (in MeV) calculated with the nonlinear effective interactions PK1, PK1R, and density-dependent meson-nucleon coupling effective interaction PKDD are shown in comparison with those of TM1 [20], NL3 [45], TW99 [24], DD-ME1 [25], and experimental data [48]. The bold-faced quantities denote the observables used in the parametrizations.

Nucleus	Expt.	PK1	PK1R	PKDD	TM1	NL3	TW99	DD-ME1
^{16}O	−127.619	**−128.094**	**−128.047**	**−127.808**	−128.951	**−127.127**	**−128.147**	**−127.926**
^{24}O	−168.500	−169.558	−169.381	−168.542	−168.858	−170.116	**−167.693**	−167.949
^{40}Ca	−342.052	**−342.773**	**−342.741**	**−342.579**	**−344.661**	**−341.709**	**−343.352**	**−343.653**
^{48}Ca	−415.991	**−416.077**	**−415.974**	**−415.944**	**−415.668**	**−415.377**	**−416.888**	**−415.012**
^{56}Ni	−483.998	**−483.956**	**−484.031**	**−484.479**	−480.620	−483.599	**−487.096**	−480.869
^{58}Ni	−506.454	−504.033	−504.091	−504.013	**−501.933**	**−503.395**	−506.128	−501.312
^{68}Ni	−590.430	**−591.685**	**−591.559**	**−591.241**	−591.845	−591.456	−592.676	−592.253
^{90}Zr	−783.893	**−784.781**	**−784.788**	**−784.879**	**−785.281**	**−783.859**	**−786.625**	**−784.206**
^{112}Sn	−953.529	−954.210	−954.251	−953.730	−955.925	−952.562	−954.991	**−952.468**
^{116}Sn	−988.681	**−988.491**	**−988.460**	**−988.066**	**−990.083**	**−987.699**	−989.842	**−988.470**
^{124}Sn	−1049.963	−1049.162	−1048.948	−1048.113	**−1049.832**	**−1049.884**	−1051.033	**−1049.880**
^{132}Sn	−1102.920	**−1103.503**	**−1103.053**	**−1102.648**	−1102.163	**−1105.459**	−1108.363	**−1103.857**
^{184}Pb	−1431.960	−1435.548	−1435.706	−1435.477	**−1439.768**	−1434.569	−1436.761	−1434.569
^{194}Pb	−1525.930	**−1525.536**	**−1525.494**	**−1525.474**	−1528.378	−1525.733	−1529.309	−1524.937
^{196}Pb	−1543.250	−1542.592	−1542.502	−1542.545	**−1545.163**	−1543.085	−1547.012	−1542.262
^{204}Pb	−1607.520	−1607.851	−1607.545	−1607.770	−1609.477	−1609.906	−1608.246	**−1609.676**
^{208}Pb	−1636.446	**−1637.443**	**−1637.024**	**−1637.387**	**−1638.777**	**−1640.584**	**−1644.790**	**−1641.415**
^{214}Pb	−1663.298	−1659.382	−1658.718	−1656.084	**−1663.706**	**−1662.551**	−1656.086	**−1662.011**
^{210}Po	−1645.228	−1648.443	−1648.102	−1648.039	−1650.819	−1650.755	−1654.271	**−1651.482**
Δ[a]		7.1980	7.4207	9.2744	12.8135	9.1140	17.6762	11.1580
δ[b]		0.0102	0.0094	0.0080	0.0192	0.0135	0.0159	0.0152

[a]The total square deviation from the experimental values $\Delta^2 = \Sigma_i (E_i^{\rm expt} - E_i^{\rm calc})^2$.
[b]The relative square deviation $\delta^2 = \Sigma_i (E_i^{\rm expt} - E_i^{\rm calc})^2/(E_i^{\rm expt})^2$.

TABLE IV. Charge radii (in femtometer) calculated with the nonlinear effective interactions PK1, PK1R, and density-dependent meson-nucleon coupling effective interaction PKDD are shown in comparison with those of TM1 [20], NL3 [45], TW99 [24], DD-ME1 [25], and experimental data [50].

Nucleus	Exp.	PK1	PK1R	PKDD	TM1	NL3	TW99	DD-ME1
^{16}O	2.693	2.6957	2.6959	2.6988	2.7026	2.7251	2.6799	2.7268
^{24}O		2.8106	2.8108	2.8184	2.8364	2.8286	2.8049	2.8543
^{40}Ca	3.478	3.4433	3.4435	3.4418	3.4541	3.4679	3.4151	3.4622
^{48}Ca	3.479	3.4675	3.4675	3.4716	3.4911	3.4846	3.4510	3.4946
^{56}Ni		3.7085	3.7084	3.7162	3.7471	3.7122	3.6867	3.7315
^{58}Ni	3.776	3.7383	3.7381	3.7442	3.7755	3.7435	3.7158	3.7613
^{68}Ni		3.8621	3.8620	3.8681	3.8901	3.8773	3.8491	3.8926
^{90}Zr	4.270	4.2522	4.2521	4.2534	4.2799	4.2689	4.2278	4.2725
^{112}Sn	4.593	4.5704	4.5701	4.5722	4.6021	4.5861	4.5461	4.5901
^{116}Sn	4.625	4.5984	4.5981	4.6004	4.6303	4.6149	4.5758	4.6212
^{124}Sn	4.677	4.6536	4.6533	4.6567	4.6874	4.6685	4.6331	4.6781
^{132}Sn		4.7064	4.7061	4.7102	4.7442	4.7183	4.6842	4.7270
^{184}Pb		5.3806	5.3801	5.3807	5.4156	5.3996	5.3511	5.4002
^{194}Pb	5.442	5.4327	5.4322	5.4329	5.4712	5.4506	5.4017	5.4539
^{196}Pb	5.449	5.4438	5.4433	5.4440	5.4826	5.4614	5.4123	5.4645
^{204}Pb	5.482	5.4869	5.4864	5.4877	5.5261	5.5027	5.4837	5.5038
^{208}Pb	5.504	5.5048	5.5043	5.5053	5.5444	5.5204	5.4750	5.5224
^{214}Pb	5.559	5.5658	5.5653	5.5635	5.6052	5.5820	5.5603	5.5779
^{210}Po		5.5370	5.5365	5.5371	5.5762	5.5539	5.5070	5.5544
Δ[a]		0.0708	0.0712	0.0655	0.0941	0.0625	0.1436	0.0588
δ[b]		0.0178	0.0179	0.0166	0.0185	0.0169	0.0346	0.0163

[a]The total square deviation from the experimental values $\Delta^2=\Sigma_i(r_i^{\rm expt}-r_i^{\rm calc})^2$.
[b]The relative square deviation $\delta^2=\Sigma_i(r_i^{\rm expt}-r_i^{\rm calc})^2/(r_i^{\rm expt})^2$.

In order to compare with the experimental nuclear binding energy of a nucleus, the calculated energy

$$E = E_{\rm rmf} + E_{\rm c.m.} + E_{\rm pair} \tag{11}$$

is obtained from the mean field contribution by adding corrections due to the center-of-mass and pairing effects for open shell nuclei. The mean field contribution $E_{\rm rmf}$ is derived from a spatial integration of the energy density given by the time components of the energy-momentum tensor. In the nonlinear (NL) self-coupling case, it reads

$$E_{\rm rmf}^{\rm NL} = \sum_{a=1}^{A} \varepsilon_a \langle \bar{\phi}_a \gamma^0 \phi_a \rangle + \int_V d^3r \Big\{ -\frac{1}{2} g_\sigma \sigma \rho_s - \frac{1}{6} g_2 \sigma^3 - \frac{1}{4} g_3 \sigma^4 \Big\} + \int_V d^3r \Big\{ -\frac{1}{2} g_\omega \omega \rho_b + \frac{1}{4} c_3 \omega^4 - \frac{1}{2} g_\rho \rho \rho_b^{(3)} + \frac{1}{4} d_3 \rho^4 - \frac{1}{2} e A_0 \rho_b^p \Big\}, \tag{12}$$

where ϕ_a denotes the single-particle spinor in the nucleus. In

TABLE V. Nuclear matter properties calculated with the nonlinear effective interactions PK1, PK1R, and the density-dependent effective interactions PKDD are shown in comparison with TM1 [20], NL3 [45], TW99 [24], and DD-ME1 [25].

Interaction	$\rho_{\rm sat}$ (fm^{-3})	E_b (MeV)	K (MeV)	J (MeV)	$M^*/M(n)$	$M^*/M(p)$
PK1	0.148195	−16.268	282.644	37.641	0.605525	0.604981
PK1R	0.148196	−16.274	283.674	37.831	0.605164	0.604620
PKDD	0.149552	−16.267	262.181	36.790	0.571156	0.570565
NL3	0.145115	−16.005	267.998	36.558	0.603761	0.603761
TM1	0.145218	−16.263	281.161	36.892	0.634395	0.634395
TW99	0.153004	−16.247	240.276	32.767	0.554913	0.554913
DD-ME1	0.151962	−16.201	244.719	33.065	0.577960	0.577960

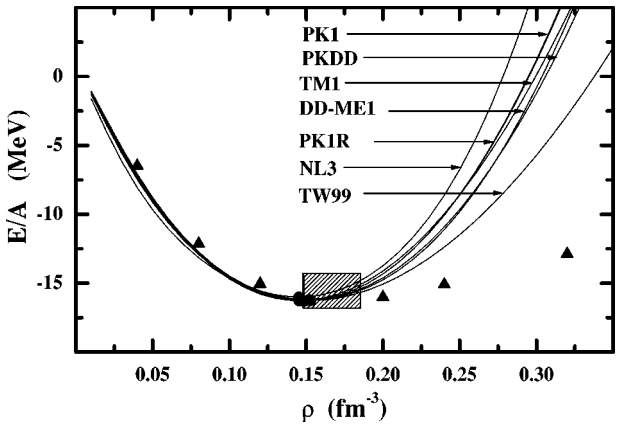

FIG. 3. The binding energy per particle E/A in nuclear matter as function of the baryonic density ρ, calculated with the density-dependent meson-nucleon coupling effective interactions PKDD, TW99, DD-ME1 and the nonlinear effective interactions PK1, PK1R, TM1, NL3. The shaded area indicates the empirical value and the filled circles represent corresponding saturation points. The filled triangle presents the data taken from Ref. [49] as comparison.

the DD case, the high-order ($\geqslant 3$) terms of mesons in Eq. (12) are replaced by a "rearrangement" term,

$$E_{\mathrm{rmf}}^{\mathrm{DD}} = \sum_{a=1}^{A} \varepsilon_a \langle \bar{\phi}_a \gamma^0 \phi_a \rangle + \int_V d^3r \Bigg\{ -\frac{1}{2} g_\sigma \sigma \rho_s - \frac{1}{2} g_\omega \omega \rho_b - \frac{1}{2} g_\rho \rho \rho_b^{(3)} - \frac{1}{2} e A_0 \rho_b^p - \Sigma_R \rho_b \Bigg\}, \tag{13}$$

where

$$\Sigma_R = \frac{1}{\rho_{\mathrm{sat}}} [g_\omega(\rho_{\mathrm{sat}}) f'_\omega(x) \rho_0 \omega - a_\rho g_\rho(\rho_{\mathrm{sat}}) e^{-a_\rho(x-1)} \rho_0^{(3)} \rho_3 + g_\sigma(\rho_{\mathrm{sat}}) f'_\sigma(x) \rho_s \sigma] \tag{14}$$

is the time component of Σ_R^μ [see Eq. (8)].

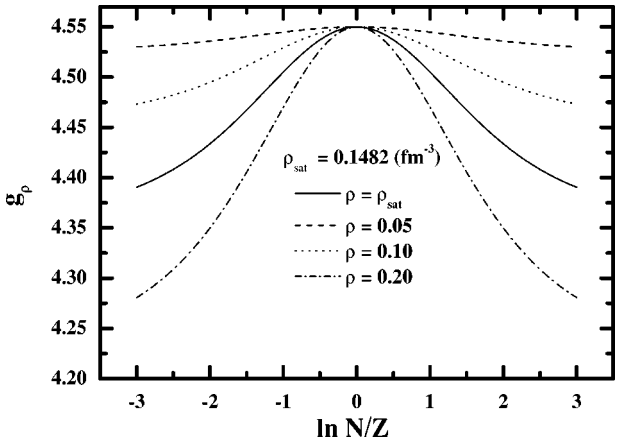

FIG. 4. The density dependence of g_ρ for PK1R with respect to the neutron-proton ratio N/Z.

C. Center-of-mass correction and pairing correlation

The correction from the center-of-mass motion is calculated from the projection after variation in first-order approximation [46]:

$$E_{\mathrm{c.m.}}^{\mathrm{mic}} = -\frac{1}{2MA} \langle \mathbf{P}_{\mathrm{c.m.}}^2 \rangle, \tag{15}$$

where the center-of-mass momentum $\mathbf{P}_{\mathrm{c.m.}} = \Sigma_i^A \mathbf{p}_i$ and the expectation value of its square $\langle \hat{\mathbf{P}}_{\mathrm{c.m.}}^2 \rangle$ reads

$$\langle \mathbf{P}_{\mathrm{c.m.}}^2 \rangle = \sum_a v_a^2 p_{aa}^2 - \sum_{a,b} v_a^2 v_b^2 \mathbf{p}_{ab} \cdot \mathbf{p}_{ab}^* + \sum_{a,b} v_a u_a v_b u_b \mathbf{p}_{ab} \cdot \mathbf{p}_{\bar{a}\bar{b}} \tag{16}$$

with the occupation probabilities v_a^2 and $u_a^2 = 1 - v_a^2$ accounting for pairing effects, where a, b denote the BCS states (see below).

The prescription (15) is based on nonrelativistic considerations. It must be noted that it does not preserve Lorentz invariance. Furthermore, it also breaks the complete self-consistence of the variational scheme since it is not included in the self-consistent procedure. Compared with the binding energy, this center-of-mass correction is sizable in light nuclei (about 9% in ^{16}O) but much less important in medium and heavy nuclei (about 0.4% in ^{208}Pb) as we have seen in Fig. 1.

For the nuclear radii, the effects from the center-of-mass motion are also taken into account as follows. Because of its fairly small effects, a rather rough correction is adopted for protons

$$\delta R_p^2 = -\frac{2}{Z} \sum_a^A \langle \phi_a | \mathbf{R}_{\mathrm{c.m.}} \cdot \sum_i^Z \mathbf{r}_i | \phi_a \rangle + \sum_a^A \langle \phi_a | \mathbf{R}_{\mathrm{c.m.}}^2 | \phi_a \rangle, \tag{17}$$

where the center-of-mass coordinate $\mathbf{R}_{\mathrm{c.m.}} = 1/A \Sigma_i^A \mathbf{r}_i$. Then we get

$$\delta R_p^2 = -\frac{2}{A} R_p^2 + \frac{1}{A} R_M^2, \tag{18}$$

where R_p and R_M denote the proton and matter radii. Here we only consider the direct-term contributions in Eq. (17) to keep with the spirit of RMF theory. For the neutron radii, we use the same procedure as for protons. The charge radius is obtained from the proton radius combining with the proton and neutron size, and the center-of-mass correction (18) is included in R_p^2 [20],

$$R_{\mathrm{ch}}^2 = R_p^2 + (0.862\ \mathrm{fm})^2 - (0.336\ \mathrm{fm})^2 N/Z. \tag{19}$$

The contribution from the pairing correlations E_{pair} are treated in the BCS approximation,

$$E_{\mathrm{pair}} = -\Delta \sum_a v_a u_a, \tag{20}$$

with the pairing gap Δ taken from the calculation of relativistic continuum Hartree-Bogoliubov (RCHB) theory with zero-range pairing interaction [32].

TABLE VI. Total binding energies of Pb isotopes (in MeV) calculated with the nonlinear self-coupling effective interactions PK1, PK1R, and the density-dependent meson-nucleon coupling effective interaction PKDD, in comparison with the experimental values [48] and the results of TM1, NL3, TW99, and DD-ME1.

A	Expt.	PK1	PK1R	PKDD	TM1	NL3	TW99	DD-ME1
182	−1411.650	−1416.431	−1416.619	−1416.309	−1420.872	−1415.184	−1417.202	−1415.216
184	−1431.960	−1435.548	−1435.706	−1435.477	−1439.768	−1434.569	−1436.761	−1434.569
186	−1451.700	−1454.258	−1454.382	−1454.192	−1458.222	−1453.511	−1455.879	−1453.306
188	−1470.900	−1472.586	−1472.673	−1472.504	−1476.272	−1472.056	−1474.640	−1471.639
190	−1489.720	−1490.555	−1490.603	−1490.468	−1493.958	−1490.247	−1493.109	−1489.657
192	−1508.120	−1508.197	−1508.201	−1508.116	−1511.317	−1508.130	−1511.329	−1507.411
194	−1525.930	−1525.536	−1525.494	−1525.474	−1528.378	−1525.733	−1529.309	−1524.937
196	−1543.250	−1542.592	−1542.502	−1542.545	−1545.163	−1543.085	−1547.012	−1542.262
198	−1560.070	−1559.378	−1559.236	−1559.329	−1561.685	−1560.199	−1564.338	−1559.403
200	−1576.365	−1575.893	−1575.697	−1575.831	−1577.942	−1577.076	−1581.344	−1576.365
202	−1592.202	−1592.095	−1591.843	−1592.022	−1593.905	−1593.679	−1598.084	−1593.133
204	−1607.520	−1607.851	−1607.545	−1607.770	−1609.477	−1609.906	−1614.197	−1609.676
206	−1622.340	−1623.126	−1622.765	−1623.167	−1624.530	−1625.725	−1630.122	−1625.966
208	−1636.446	−1637.443	−1637.024	−1637.387	−1638.777	−1640.584	−1644.790	−1641.415
210	−1645.568	−1644.844	−1644.345	−1643.643	−1647.245	−1647.969	−1650.888	−1648.312
212	−1654.524	−1652.155	−1651.573	−1649.873	−1655.549	−1655.289	−1657.020	−1655.174
214	−1663.298	−1659.382	−1658.718	−1656.084	−1663.706	−1662.551	−1663.196	−1662.011

III. PARAMETRIZATION OF EFFECTIVE LAGRANGIAN AND NUMERICAL DETAILS

The aim of the present investigation is to provide new improved effective interactions for the Lagrangian density (1) with the nonlinear self-coupling and density-dependent meson-nucleon coupling in RMF theory. A multiparameter fitting was performed with the Levenberg-Marquardt method [47]. Two nonlinear self-coupling effective interactions have been obtained, PK1 with σ- and ω-meson self-coupling, and PK1R with σ-, ω-, and ρ-meson self-coupling (see Table I).

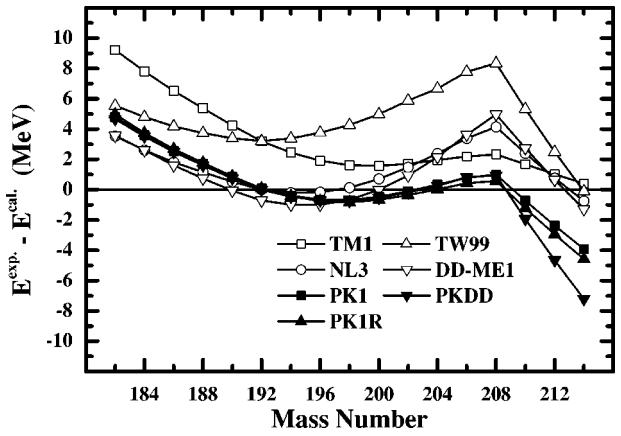

FIG. 5. The deviation of the theoretical binding energies of Pb isotopes, calculated with the nonlinear effective interactions PK1, PK1R and density-dependent meson-nucleon coupling effective interactions PKDD from the experimental values [48]. The results calculated in TM1, NL3 and TW99, DD-ME1 are shown for comparison.

A density-dependent meson-nucleon coupling effective interaction has also been obtained with PKDD (see Tables I and II). In our parametrization, the masses of neutron and proton are fixed to their free values: M_n=939.5731 MeV and M_p =938.2796 MeV, and the mass of ρ meson is fixed to its experimental value 763.0 MeV. The mass of ω meson is slightly adjusted in obtaining the effective interactions PK1 and PK1R while fixed to 783.0 MeV for the effective interaction PKDD.

The masses of the spherical nuclei ^{16}O, ^{40}Ca, ^{48}Ca, ^{56}Ni, ^{68}Ni, ^{90}Zr, ^{116}Sn, ^{132}Sn, ^{194}Pb, and ^{208}Pb are fitted to give the effective interactions PK1, PK1R, and PKDD. The experimental inputs for finite nuclei used in the fitting procedure are shown in Table III. These inputs have been used to minimize the least square error:

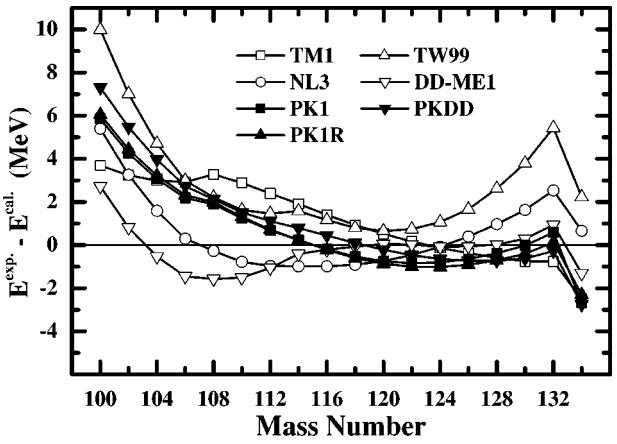

FIG. 6. Same as Fig. 5, for Sn isotopes.

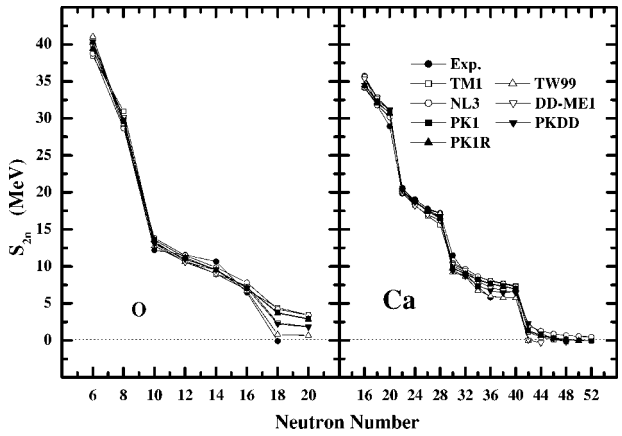

FIG. 7. The two-neutron separation energies in O and Ca isotopes calculated with the nonlinear effective interactions PK1, PK1R, and the density-dependent meson-nucleon effective interaction PKDD, in comparison with those of TM1, NL3, TW99, and DD-ME1, and the experimental data [48].

$$\chi^2(\mathbf{a}) = \sum_{i=1}^{N} \left[\frac{y_i^{expt} - y(x_i;\mathbf{a})}{\sigma_i} \right]^2, \qquad (21)$$

where **a** is the ensemble of parameters to be fitted, y_i^{expt} and σ_i are the experimental observable and corresponding weight.

In the fitting procedure, only the masses of the spherical nuclei mentioned above, the compression modulus K, the baryonic density at saturation ρ_{sat}, and the asymmetry energy J of nuclear matter are included. Here, we should mention that the radii are excluded because we found that the values of the compression modulus and baryonic saturation density are essential to give a good description of the masses and radii. For a fixed value of compression modulus, a large baryonic saturation density will give a small charge radius. By this way, we can choose the appropriate value for these two quantities to give a proper description for both mass and charge radius of the chosen nuclei. To give a fairly precise description on the masses, the center-of-mass correction is essential for both light and heavy nuclei. As it can be seen in Fig. 1, the deviation between the microscopic and phenomenological results is considerably large not only for the light nuclei but also for the heavy ones. We also find that there exist very remarkable shell effects in the microscopic results which are impossible to obtain with the phenomenological methods. Hence, we choose the microscopic center-of-mass correction [46] to deal with the center-of-mass motion.

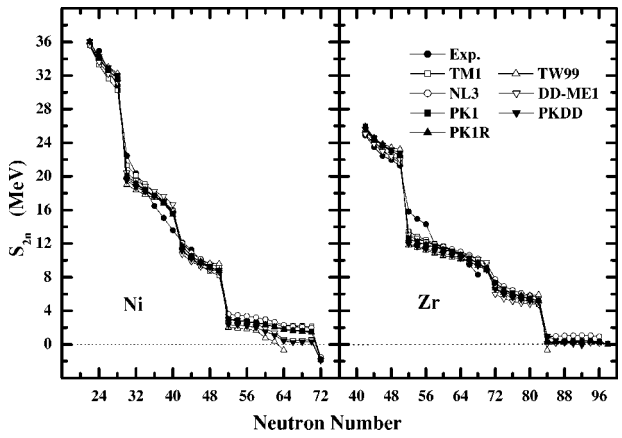

FIG. 8. Same as Fig. 7, for Ni and Zr isotopes.

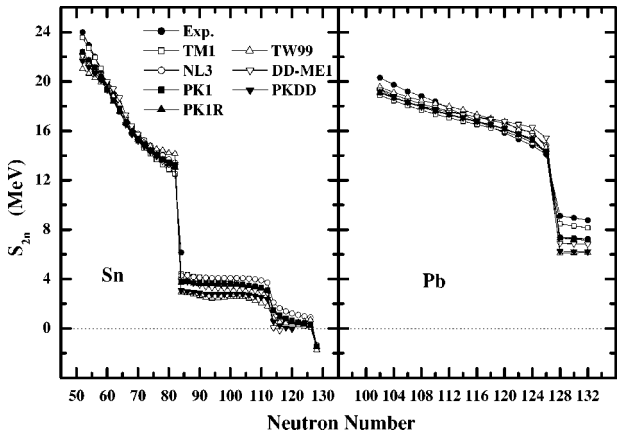

FIG. 9. Same as Fig. 7, for Sn and Pb isotopes.

The numerical procedure in obtaining the parameter set PK1 is as follows.

(1) First, we start from an initial effective interaction and fix the mass of ω meson, let the other parameters to be adjusted by the Levenberg-Marquardt method [47].

(2) Basing on the binding energies and charge radii of the selected nuclei obtained in the first step, we do some adjustment on the expectation of compression modulus and baryonic saturation density to improve the description on the spherical nuclei. Also, the weights of the observables would be slightly adjusted to improve the parametrization.

(3) Choose another initial effective interaction and take the same procedure as in step 2. Then, taking the average of these two obtained interactions as the new initial effective interaction, we do the minimizing procedure under the new weights which come from the previous results.

(4) Introduce the adjustment on the mass of ω meson to obtain the effective interaction PK1.

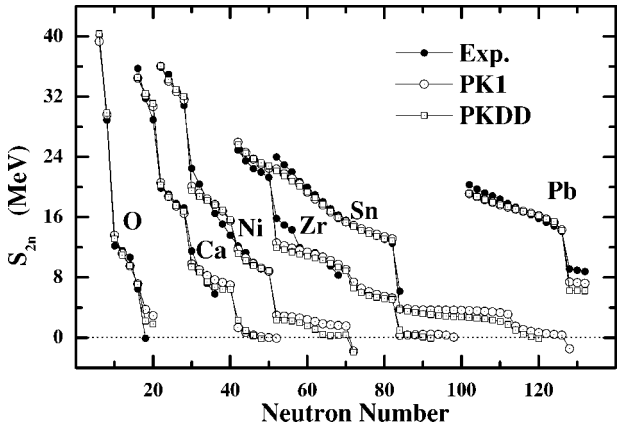

FIG. 10. The two-neutron separation energies calculated with the nonlinear effective interaction PK1 and the density-dependent meson-nucleon coupling one PKDD, as a function of the neutron number.

TABLE VII. Charge radii of Pb isotopes (in femtometer), calculated with the nonlinear effective interactions PK1, PK1R, and the density-dependent meson-nucleon coupling effective interaction PKDD, in comparison with those of TM1, NL3, TW99, DD-ME1, and experimental values [50,51].

A	Expt.	PK1	PK1R	PKDD	TM1	NL3	TW99	DD-ME1
190	5.4273	5.4112	5.4107	5.4115	5.4486	5.4295	5.3814	5.4325
192	5.4347	5.4219	5.4214	5.4221	5.4599	5.4400	5.3915	5.4433
194	5.4416	5.4327	5.4322	5.4329	5.4712	5.4506	5.4017	5.4539
196	5.4487	5.4438	5.4433	5.4440	5.4826	5.4614	5.4123	5.4645
198	5.4564	5.4551	5.4546	5.4555	5.4940	5.4722	5.4241	5.4748
200	5.4649	5.4664	5.4659	5.4673	5.5052	5.4830	5.4366	5.4850
202	5.4741	5.4773	5.4768	5.4786	5.5161	5.4934	5.4493	5.4947
204	5.4820	5.4869	5.4864	5.4877	5.5261	5.5027	5.4571	5.5038
206	5.4930	5.4954	5.4949	5.4960	5.5352	5.5109	5.4653	5.5125
208	5.5040	5.5048	5.5043	5.5053	5.5444	5.5204	5.4750	5.5224
210	5.5231	5.5252	5.5247	5.5247	5.5645	5.5411	5.4935	5.5409
212	5.5415	5.5455	5.5450	5.5441	5.5846	5.5616	5.5122	5.5594
214	5.5591	5.5658	5.5653	5.5635	5.6052	5.5820	5.5310	5.5779

Because the contribution to the nuclear mass from the nonlinear ρ-meson term is fairly small, we fix the nonlinear self-coupling constant d_3 to 350.0 and adjust other parameters to obtain the effective interaction PK1R.

To obtain the density-dependent meson-nucleon coupling effective interaction PKDD, we leave the density-dependent parameters a_σ, d_σ, and d_ω to be adjusted and the five others to be determined by the constrain conditions on the functions $f_i(x), i=\sigma,\omega$. The mass of ω meson is fixed to 783.0 MeV.

Thus obtained parameter sets are shown in Tables I and II in comparison with other effective interactions TM1 [20], NL3 [45], TW99 [24], and DD-ME1 [25]. In Tables III and IV we list the masses and charge radii, respectively, of finite nuclei which have been used in obtaining these seven effective interactions. Compared with other effective interactions, our newly obtained ones reproduce well the experimental masses [48]. For these new effective interactions, only 4–5 nuclear masses deviate by more than 1 MeV (see Table III). The new effective interactions PK1, PK1R, and PKDD also well describe the charge radii for these nuclei, especially for Pb isotopes. One can get a clear idea about the improvement of the new parameter sets on the description of bulk properties for finite nuclei from the root of relative square (rrs) deviation δ. In the last row of Table III (IV), the rrs deviation of the calculated total binding energy (charge radius) from the data is given. For the total binding energy, the rrs deviations from the new parameter sets are much smaller than those from old ones. For the charge radius, the rrs deviations from the new interactions are comparable with those from NL3 and DD-ME1, but a bit smaller than those from TM1 and TW99.

Table V lists the nuclear matter quantities calculated with the newly obtained effective interactions PK1, PK1R, and PKDD, in comparison with other interactions. All the new effective interactions give proper value of the compression

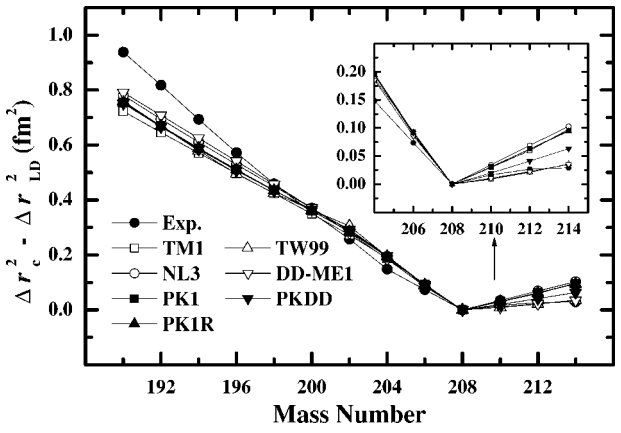

FIG. 11. The isotope shifts of the charge radius in Pb isotopes (in fm^2), calculated with the nonlinear effective interactions PK1, PK1R, and the density-dependent meson-nucleon coupling effective interaction PKDD, in comparison with those of TM1, NL3, TW99, DD-ME1, and experimental values, where $\Delta r_c^2 = r_c^2(A) - r_c^2(208)$ and $\Delta r_{LD}^2 = r_{LD}^2(A) - r_{LD}^2(208)$.

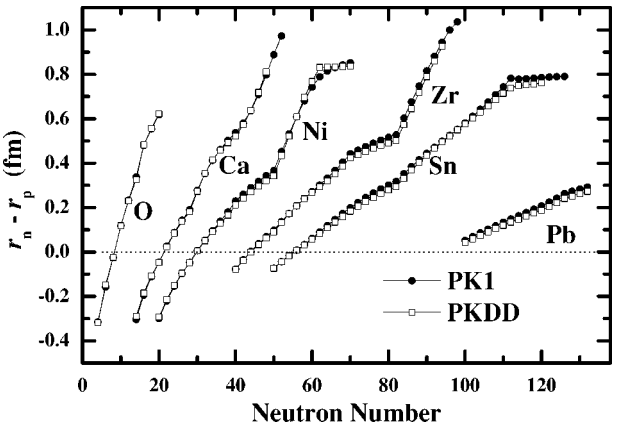

FIG. 12. The radius difference $r_n - r_p$ calculated with the nonlinear effective interaction PK1 and density-dependent meson-nucleon coupling one PKDD, with respect to the neutron number.

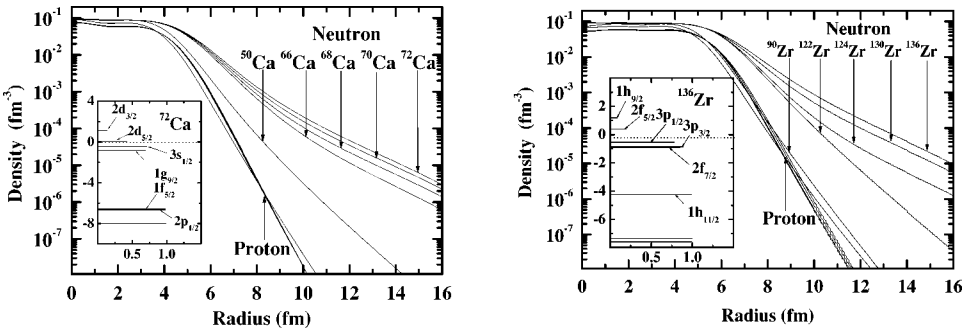

FIG. 13. Density distributions of Ca isotopes and Zr isotopes. The small figures inside show the configurations and occupations near the Fermi surface where the dot lines present the Fermi surface.

modulus K. Compared with the nonlinear self-coupling effective interactions TM1 [20] and NL3 [45], the new ones give more reasonable baryonic saturation density.

IV. DESCRIPTION OF NUCLEAR MATTER

We first discuss properties of nuclear matter obtained with PK1, PK1R, and PKDD. In Table V we compare the bulk properties of nuclear matter with the results calculated using TM1, NL3, TW99, and DD-ME1. In Fig. 3, the behavior of the binding energy per particle E/A as a function of the baryonic density ρ is shown. We can see that all density-dependent meson-nucleon coupling effective interactions give softer results than the nonlinear self-coupling ones. The behaviors predicted by PK1 and PK1R are much softer than by NL3 and a little harder than by TM1. The results from PKDD are slightly softer than those from DD-ME1 and much harder than those from TW99 at high density. All these behaviors can be explained in the density-dependent meson-nucleon coupling framework. The nonrelativistic calculation for the symmetric nuclear matter [49] is also given in Fig. 3 as comparison, which predicts much softer behavior than relativistic ones.

As we have mentioned in expressions (10), the meson-nucleon coupling constants in the nonlinear self-coupling of mesons can be expressed as some kind of density dependence. Figure 2 shows this density dependence for the nonlinear self-coupling effective interactions and the results for the density-dependent version are also given for comparison. We can see that almost all the density-dependent coupling constants decrease with increasing density except for g_σ of NL3, which has a strong σ self-coupling ($g_3=-28.8851$). On the other hand, the coupling constants g_σ and g_ω of TM1, which has relatively weak σ self-coupling ($g_3=0.6183$) and strong ω self-coupling ($c_3=71.3075$), are smaller than the others, which means that TM1 provides relatively weaker scalar and vector potentials. This is the reason why TM1 presents the softer behavior than other nonlinear self-coupling effective interactions. In Fig. 3, TW99 predicts the softest results because of its relatively small g_ω as compared with DD-ME1, PKDD, and NL3, and large g_σ as compared with PK1, PK1R, and TM1 in Fig. 2. As we know, the repulsive potential would be dominant at high density. In Fig. 3, NL3 gives the hardest results because of its constant and large g_ω even though its σ-N coupling constant g_σ increases with the density. For the new parameter sets PK1, PK1R, and PKDD, which present the mid soft behaviors in Fig. 3, the coupling constants also lie between the largest and the smallest in Fig. 2. For the parameter set PK1R, the density dependence of the g_ρ is fairly weak as compared with that of the density-dependent meson-nucleon coupling effective interactions. It can be explained by a very weak ρ field, which generates neutron-proton symmetry field. The behavior of g_ρ with respect to the neutron-proton ratio is shown in Fig. 4. As one can expect, the behavior is symmetric with respect to $\ln(N/Z)$ and the density dependence becomes more remarkable with the increase of the baryonic density and the neutron-proton asymmetry.

V. DESCRIPTION OF SPHERICAL NUCLEI

A. Binding energy and two-neutron separation energy

We calculate the even-even nuclei of Pb and Sn isotopic chains with the newly obtained parameter sets. In Table VI, we compare the masses calculated with PK1, PK1R, and PKDD with the other effective interactions and with experimental values [48]. Shown in Fig. 5 are the deviations of the masses of Pb isotopes from the data [48]. The results for Sn isotopes are shown in Fig. 6. In Figs. 5 and 6 we also give the results obtained with TM1, NL3, TW99, and DD-ME1

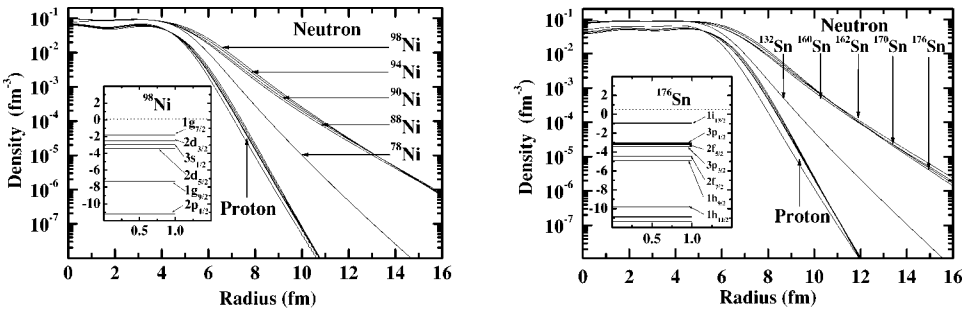

FIG. 14. Same as Fig. 13, for Ni and Sn isotopes.

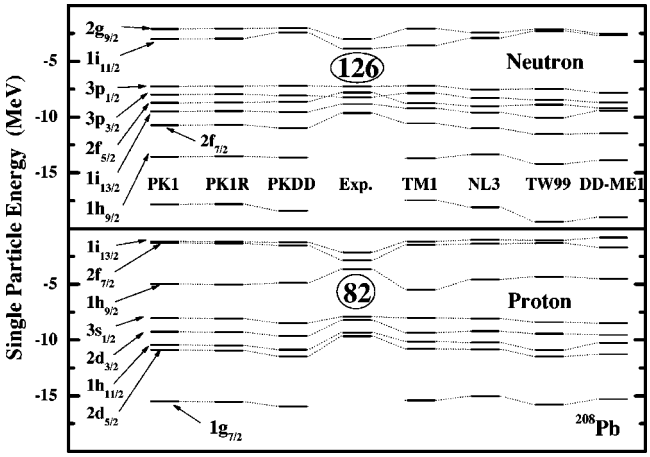

FIG. 15. The single-particle energies in ^{208}Pb, calculated with PK1, PK1R, and PKDD, in comparison with the results of TM1, NL3, TW99, DD-ME1, and experimental values.

for comparison. All results are calculated using the RCHB theory [32] where the pairing correlations are treated self-consistently by a zero-range δ force. The box radius is 20 fm and the pairing strength of the zero-range δ force is −650 MeV. The microscopic center-of-mass corrections (15) and (16) are used in all the calculations.

As we can see in Table VI and Figs. 5 and 6, the newly obtained effective interactions PK1, PK1R, and PKDD provide good descriptions on the masses of both isotopic chains. In Fig. 5, all the effective interactions overestimate the binding energy in the beginning of the isotopic chain. However, from ^{190}Pb to ^{210}Pb, the newly obtained interactions give better descriptions than all the others. For the Sn isotopes, the density-dependent effective interaction DD-ME1 reproduces the data very well since four Sn isotopes were used in its parametrization [25]. From ^{116}Sn to ^{132}Sn, the new effective interactions PK1, PK1R, and PKDD slightly underestimate the binding energy (less than 1 MeV). Compared with the others, the new ones still provide a better description. There exist however systematic deviations out of the neutron magic numbers, e.g., in ^{134}Sn and ^{214}Pb. For the older effective interactions, the deviations in ^{214}Pb are smaller but fairly large in ^{208}Pb.

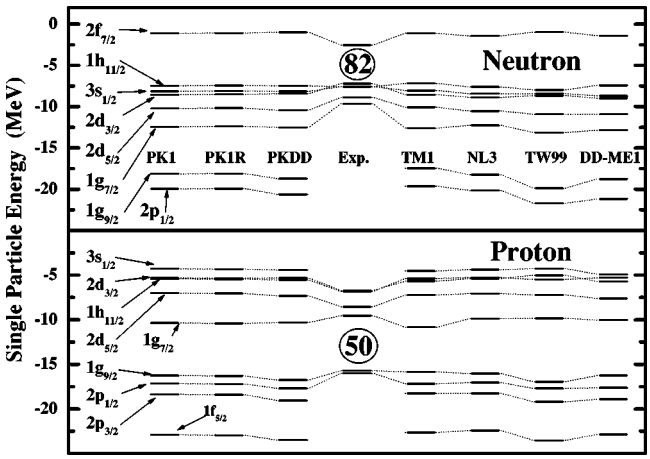

FIG. 16. Same as Fig. 15, for ^{132}Sn.

From the binding energies we can extract the systematics in two-neutron separation energies $S_{2n}=E_B(N,Z)-E_B(N-2,Z)$. Figures 7–9 exhibit two-neutron separation energies predicted by the nonlinear self-coupling effective interactions PK1, PK1R, and the density-dependent meson-nucleon coupling one PKDD. In comparison, the results obtained with TM1, NL3, TW99, and DD-ME1 and the experimental values extracted from Ref. [48] are also given. In Fig. 10, the systematic behaviors of two-neutron separation energies with respect to neutron number, predicted by the new effective interactions PK1 and PKDD, are shown. From these figures one can see that the newly obtained interactions give a fairly good description on the systematic behaviors in two-neutron separation energies. In Fig. 8, we can see that the deviations of theoretical results from experiment are rather large for Ni isotopes with $N=30-42$ and for Sn isotopes with $N=52-58$. Here it should be mentioned that all the theoretical results are extracted from the calculation of the spherical RCHB calculations [32] where deformation effects are not included while they can play a significant role in these nuclei. Furthermore, in Fig. 10 we can see some unusual phenomena along the neutron drip line which will be discussed in the following section.

From the plots for two-neutron separation energies (Figs. 7–10), the position of the neutron-drip line for each element seems to be determined delicately. For the new effective interaction PK1, it predicts the neutron-drip number $N=50$ for Ca, 70 for Ni, 96 for Zr, and 126 for Sn. In general, the density-dependent meson-nucleon coupling effective interaction PKDD predicts smaller neutron number of the neutron-drip nucleus except for Ni. This may be due to its fairly small effective mass (see Table V), which reduces the strong attractive potential in the core and makes the coupling between the core and valence orbital weaker. As for the density-dependent effective interactions, TW99 predicts smaller neutron numbers of neutron-drip nucleus for Ca, Ni, and Zr while DD-ME1 gives smaller ones for Ca and Sn. Another reason for the deviations among the effective interactions is that the density-dependent effective interactions give relatively large ρ-N coupling at lower densities (see Fig. 2).

B. Charge radii and neutron distributions

Although the radii are not included in our fitting procedure, the newly obtained effective interactions reproduce the charge radii of stable nuclei fairly well (see Table IV). The comparison between experimental data [50,51] and theoretical results for the charge radii (19) of Pb isotopes are shown in Table VII. We can see that the new effective interactions PK1, PK1R, and PKDD reproduce better the experimental values, as compared to overestimations by TM1, NL3, and DD-ME1 and underestimations by TW99. We also calculate the isotope shift of charge radii for Pb isotopes with these effective interactions. The results are shown in Fig. 11. The kink around ^{208}Pb is well reproduced by all the interactions. The inset of Fig. 11 shows that the density-dependent meson-nucleon coupling effective interactions represent more reasonable agreement with the experimental values than the

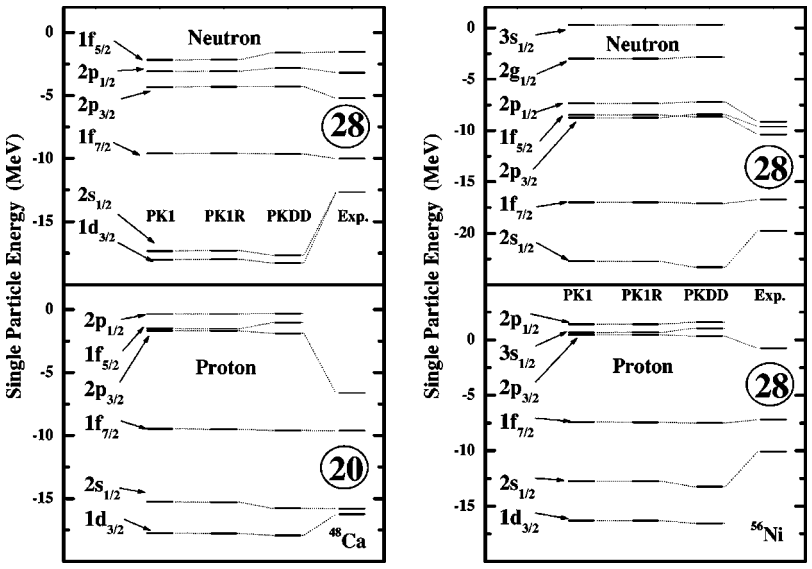

FIG. 17. The single-particle energies in ^{48}Ca and ^{56}Ni, calculated with PK1, PK1R, and PKDD, in comparison with experimental values.

nonlinear self-coupling ones. The new parameter sets PK1 and PK1R give slightly better results than TM1 and NL3.

Besides the charge radii, we have also used the new effective interactions to investigate the systematic behavior of the neutron skin (the difference between neutron and proton radii) along the isotope chains: O, Ca, Ni, Zr, Sn, and Pb. Figure 12 shows the radii difference $r_n - r_p$ calculated with the new sets PK1 and PKDD. As we have seen in Fig. 10, there are several weakly bound nuclei near the neutron-drip line of Ca, Ni, Zr, and Sn, whose two-neutron separation energies stay around zero over a range of numbers. This is in general a kind of signal for the existence of a neutron skin or halo. However from Fig. 12 one can see that the difference $r_n - r_p$ tends to be a constant near the drip line for the Ni and Sn isotopes thus indicating a neutron skin rather than a neutron halo. On the other hand, the results support the existence of a neutron halo in Ca isotopes [52] and a giant neutron halo in Zr isotopes [8] because their neutron distributions tend to be more dispersive and $r_n - r_p$ keeps increasing rapidly. These characters are also supported well by the neutron distributions in Figs. 13 and 14. In Fig. 13, it shows that the neutron distributions tend to be more extended with the increasing of neutron number. It can be well interpreted by the configurations and occupations near the Fermi surface for those drip line nuclei (see the small figures in Fig. 13). For Ca and Zr isotopes, the valence orbits of the drip line nuclei are *s* or *p* states which lead to fairly weak centrifugal potential and mainly account for the extended distributions. Whereas, Fig. 14 shows that the neutron distributions tend to be dispersive until ^{162}Sn for Sn isotopes and ^{90}Ni for Ni isotopes where the low orbits accounting for these extended distributions. After that, the valence neutrons stay in high orbit (see small figures in Fig. 14) which reduce remarkable centrifugal potential. It makes the distributions to be contractible and stops the formation of a halo structure.

C. Single-particle energy and spin-orbit splitting

The RMF theory is a microscopic theory with a limited number of parameters. It can give the detailed microscopic

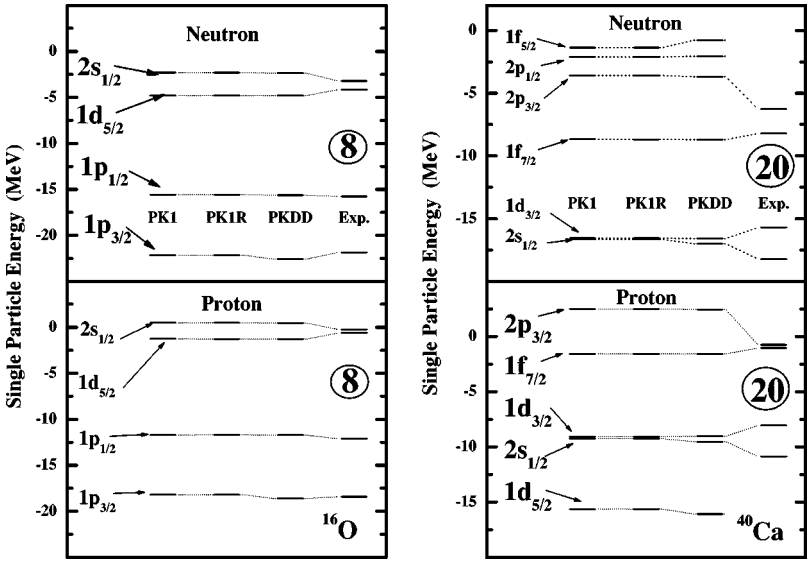

FIG. 18. Same as Fig. 17, for ^{16}O and ^{40}Ca.

TABLE VIII. The theoretical (calculated with the nonlinear effective interactions PK1, PK1R, TM1 [20], NL3 [45] and the density-dependent ones PKDD, TW99 [24], DD-ME1 [25]) and experimental spin-orbit splittings (in MeV) of neutron (ν) and proton (π) levels in doubly magic nuclei.

Nucleus	State	PK1	PK1R	PKDD	Expt.	TM1	NL3	TW99	DD-ME1
^{16}O	ν1p	6.550	6.550	6.950	6.180	5.660	6.480	7.480	6.320
	π1p	6.490	6.500	6.900	6.320	5.610	6.400	7.410	6.250
^{48}Ca	ν1f	7.411	7.417	8.028	8.380	6.486	7.493	8.687	7.498
	ν2p	1.238	1.237	1.459	2.020	1.142	1.330	1.567	1.458
^{56}Ni	ν1f	8.223	8.231	8.670	7.160	6.907	8.703	9.274	8.067
	ν2p	1.141	1.142	1.442	1.110	1.105	1.112	1.573	1.388
	ν2d	1.659	1.662	1.990	1.650	1.515	1.661	2.257	1.940
^{132}Sn	π1g	5.900	5.910	6.450	6.080	5.010	6.152	7.108	6.210
	π2d	1.704	1.706	2.005	1.750	1.556	1.690	2.203	1.893
	ν2f	2.005	2.008	2.356	1.770	1.812	2.011	2.648	2.268
	ν1i	6.492	6.503	7.126	5.840	5.634	6.665	7.761	6.748
^{208}Pb	ν3p	0.742	0.742	0.879	0.900	0.657	0.764	0.992	0.866
	π2d	1.626	1.622	1.832	1.330	1.436	1.628	2.031	1.736
	π1h	5.448	5.458	5.976	5.560	4.653	5.661	6.576	5.749

structure of nuclei. Figures 15–18 show the single-particle energies of the doubly magic nuclei calculated with the newly obtained parameter sets PK1, PK1R, and PKDD. In Figs. 15 and 16 the results obtained with TM1, NL3, TW99, and DD-ME1 are also given for comparison. As we know, it is not straightforward to compare with the experimental results away from Fermi energies because of dynamical coupling not included in RMF. Here, the experimental values are extracted from one-nucleon separation energies [48] and resonance energies [53]. In these plots, we find systematic agreements with the experimental results. The single-particle energies near the magic numbers agree well with the experimental values. For levels far away from the Fermi energies systematic deviations appear. The states below the Fermi energy seem to be too strongly bound, whereas the states above the Fermi energy show underbinding as compared to the experimental values. In fact, the experimental resonances are not simply single-particle states. The coupling with core excitations through the residual interaction, which is obviously not included in the mean field model, leads in general to a shift of the resonance energies in the direction of the Fermi energy. In these plots of single-particle energies, the ordering of levels is well described by the new effective interactions except for somewhat different ordering of neutron levels in ^{132}Sn and ^{208}Pb, a common feature of all the effective interactions.

From the single-particle energies mentioned above, we can extract the spin-orbit splittings. Table VIII shows the spin-orbit splitting calculated with the newly obtained effective interactions in the doubly magic nuclei. The experimental values and the results calculated with other interactions are also given for comparison in Table VIII. The new effective interactions reproduce well the spin-orbit splittings. For the density-dependent meson-nucleon coupling effective interaction PKDD, the spin-orbit splitting turns out to be larger than the experimental values (except for the neutron $2p$ in ^{48}Ca and the neutron $3p$ in ^{208}Pb). The nonlinear self-coupling effective interactions PK1 and PK1R predict smaller splitting and improve the agreement with the experiment. The behavior can be explained by the relatively large self-energies predicted in our parametrization, which determine the strength of spin-orbit splitting. As shown in Table V, the nonlinear self-coupling effective interactions predict a larger effective mass than the density-dependent meson-nucleon coupling ones: the smaller the effective mass, the larger the spin-orbit splitting. This is also the reason why TM1 gives the smallest splitting and TW99 the largest.

VI. SUMMARY

In this work, we have searched for new effective interactions to describe both stable and unstable nuclei in the RMF theory with nonlinear self-coupling or density-dependent meson-nucleon coupling. In order to give a more precise description on the mass of nuclei, the microscopic center-of-mass correction is introduced, which makes it possible to give a unified description with one effective interaction for the nuclei from the light area to heavy area. As an elicitation from the density-dependent meson-nucleon coupling RMF theory, we introduce the nonlinear self-coupling for ρ field. We obtain three new effective interactions: PK1 with nonlinear self-coupling of σ field and ω field, PK1R with nonlinear self-coupling of σ field, ω field, and ρ field, and PKDD with density-dependent meson-nucleon coupling.

With the newly obtained parameter sets, we investigate the behavior of the binding energy per particle and the meson-nucleon coupling constants with respect to the baryonic density in nuclear matter. The new sets PK1, PK1R, and PKDD provide an appropriate description. Compared with TM1 and NL3, the new ones give a more reasonable baryonic saturation density.

We then calculated the usual reference nuclei and Pb, Sn isotope chains and compared the masses with the available

data. The nonlinear self-coupling effective interactions PK1, PK1R, and density-dependent meson-nucleon coupling effective interaction PKDD reproduce well the data. As compared with other existing effective interactions, the new ones also provide a good description of the charge radii of the usual stable nuclei and Pb isotopes.

We have also studied the systematics of two-neutron separation energies and neutron skin in isotopic chains. The two-neutron separation energies provided by the new interactions PK1, PK1R, and PKDD are in good agreement with the experiment. We have also investigated the behavior of two-neutron separation energies and neutron skin near the neutron-drip line and given a reasonable interpretation of the formation of neutron halos.

The single-particle energies and spin-orbit splittings in doubly magic nuclei predicted by the new parameter sets are compared with the experimental values and with other effective interactions. The new effective interactions PK1, PK1R, and PKDD give a reasonable description of spin-orbit splittings and single-particle energies as compared with the experimental results. The systematic behavior of the spin-orbit splitting is interpreted in comparison with other effective interactions.

Combining with the above information, we come to a conclusion that the new parameter sets PK1, PK1R, and PKDD give a better description for finite nuclei than other effective interactions.

ACKNOWLEDGMENTS

This work was partly supported by the Major State Basic Research Development Program under Contract No. G2000077407 and the National Natural Science Foundation of China under Grants Nos. 10025522, 10047001, 10221003, and 19935030.

[1] I. Tanihata, Prog. Part. Nucl. Phys. **35**, 505 (1995).
[2] A. Mueller, Prog. Part. Nucl. Phys. **46**, 359 (2001).
[3] I. Tanihata, H. Hamagaki, O. Hashimoto, Y. Shida, N. Yoshikawa, K. Sugimoto, O. Yamakawa, T. Kobayashi, and N. Takahashi, Phys. Rev. Lett. **55**, 2676 (1985).
[4] I. Tanihata, T. Kobayashi, O. Yamakawa, S. Shimoura, K. Ekuni, K. Sugimoto, N. Takahashi, T. Shimoda, and H. Sato, Phys. Lett. B **206**, 592 (1988).
[5] R. E. Warner *et al.*, Phys. Rev. C **52**, R1166 (1995).
[6] L. Chulkov, G. Kraus, O. Bochkarev, P. Egelhof, H. Geissel, M. Golovkov, H. Irnich, and Z. Janas, Nucl. Phys. **A603**, 219 (1996).
[7] J. Meng and P. Ring, Phys. Rev. Lett. **77**, 3963 (1996).
[8] J. Meng and P. Ring, Phys. Rev. Lett. **80**, 460 (1998).
[9] J. Meng, I. Tanihata, and S. Yamaji, Phys. Lett. B **419**, 1 (1998).
[10] J. Meng, S. Zhou, and I. Tanihata, Phys. Lett. B **592**, 209 (2002).
[11] T. Kobayashi *et al.*, Phys. Lett. B **232**, 51 (1989).
[12] T. Kobayashi, Nucl. Phys. **A538**, 343c (1992).
[13] T. Alm, G. Öpke, W. Bauer, F. Daffin, and M. Schmidt, Nucl. Phys. **A587**, 815 (1995).
[14] A. Yoshida *et al.*, Nucl. Phys. **A588**, 109c (1995).
[15] J. Walecka, Ann. Phys. (N.Y.) **83**, 491 (1974).
[16] B. Serot and J. D. Walecka, Adv. Nucl. Phys. **16**, 1 (1986).
[17] P.-G. Reinhard, Rep. Prog. Phys. **52**, 439 (1989).
[18] P. Ring, Prog. Part. Nucl. Phys. **37**, 193 (1996).
[19] J. Boguta and A. Bodmer, Nucl. Phys. **A292**, 413 (1977).
[20] Y. Sugahara and H. Toki, Nucl. Phys. **A579**, 557 (1994).
[21] R. Brockmann and H. Toki, Phys. Rev. Lett. **68**, 3408 (1992).
[22] H. Lenske and C. Fuchs, Phys. Lett. B **345**, 355 (1995).
[23] C. Fuchs, H. Lenske, and H. H. Wolter, Phys. Rev. C **52**, 3043 (1995).
[24] S. Typel and H. H. Wolter, Nucl. Phys. **A656**, 331 (1999).
[25] T. Nikšić, D. Vretenar, P. Finelli, and P. Ring, Phys. Rev. C **66**, 024306 (2002).
[26] F. Hofmann, C. M. Keil, and H. Lenske, Phys. Rev. C **64**, 034314 (2001).
[27] Z. yu Ma and L. Liu, Phys. Rev. C **66**, 024321 (2002).
[28] F. Hofmann, C. M. Keil, and H. Lenske, Phys. Rev. C **64**, 025804 (2001).
[29] S. Banik and D. Bandyopadhyay, Phys. Rev. C **66**, 065801 (2002).
[30] H. Guo, Y. Chen, B. Liu, Q. Zhao, and Y. Liu, Phys. Rev. C **68**, 035803 (2003).
[31] C. Keil and H. Lenske, Phys. Rev. C **66**, 054307 (2002).
[32] J. Meng, Nucl. Phys. **A635**, 3 (1998).
[33] J. Ginocchio, Phys. Rev. Lett. **78**, 436 (1997).
[34] J. Meng, K. Sugawara-Tanabe, S. Yamaji, P. Ring, and A. Arima, Phys. Rev. C **58**, R628 (1998).
[35] J. Meng, K. Sugawara-Tanabe, S. Yamaji, and A. Arima, Phys. Rev. C **59**, 154 (1999).
[36] H. Madokoro, J. Meng, M. Matsuzaki, and S. Yamaji, Phys. Rev. C **62**, 061301 (2000).
[37] Z.-Y. Ma, A. Wandelt, N. V. Giai, D. Vretenar, P. Ring, and L.-G. Cao, Nucl. Phys. **A703**, 222 (2002).
[38] J. König and P. Ring, Phys. Rev. Lett. **71**, 3079 (1993).
[39] A. Afanasjev, J. König, and P. Ring, Nucl. Phys. **A608**, 107 (1996).
[40] A. Afanasjev, J. König, and P. Ring, Phys. Lett. B **367**, 11 (1996).
[41] J. König and P. Ring, Technical University Munich preprint, 1996.
[42] P. Reinhard, M. Rufa, J. Maruhn, W. Greiner, and J. Friedrich, Z. Phys. A **323**, 13 (1986).
[43] P.-G. Reinhard, Z. Phys. A **329**, 257 (1988).
[44] M. Sharma, M. Nagarajan, and P. Ring, Phys. Lett. B **312**, 377 (1993).
[45] G. A. Lalazissis and P. Ring, Phys. Rev. C **55**, 540 (1997).
[46] M. Bender, K. Rutz, P.-G. Reinhard, and J. A. Maruhn, Eur. Phys. J. A **7**, 467 (2000).
[47] W. H. Press, S. A. Teukolsky, W. T. Vetterling, and B. P. Flannery, *Numerical Recipes* in FORTRAN 77 (Press Syndicate of the

University of Cambridge, London, 1992).
[48] G. Audi and A. Wapstra, Nucl. Phys. **A595**, 409 (1995).
[49] A. Akmal, V. R. Pandharipande, and D. G. Ravenhall, Phys. Rev. C **58**, 1804 (1998).
[50] G. Fricke, C. Bernhardt, K. Heilig, L. Schaller, S. Schellenberg, E. Shera, and C. W. Dejager, At. Data Nucl. Data Tables **60**, 177 (1995).
[51] S. Dutta, R. Kirchner, O. Klepper, T. Kühl, D. Marx, G. Sprouse, R. Menges, U. Dinger, G. Huber, and S. Schroder, Z. Phys. A **341**, 39 (1991).
[52] J. Meng, H. Toki, J. Zeng, S. Zhang, and S. Zhou, Phys. Rev. C **65**, 041302 (2002).
[53] NUDAT database, National Nuclear Data Center (http://www.nndc.bnl.gov/nndc/nudat/).